An Experimental Characterization of Atmospheric Turbulence Effects on Millimeter-Wave Propagation in a Controlled Environment

Shawn Sheng, *Student Member, IEEE*, Omkar Pradhan, *Senior Member, IEEE*, Roni Goldshmid, Simone Tanelli, Ken Cooper, *Senior Member, IEEE*, and Azita Emami, *Senior Member, IEEE*

***Abstract*—This article introduces a novel method for experimentally characterizing atmospheric turbulence effects on millimeter-wave (mmWave) propagation in a controlled laboratory environment. A large fan array wind tunnel (FAWT) with 36 × 36 individually programmable dual-fan units is used to create turbulent flows over a controlled temperature gradient. A W-band (95.4 GHz) radar is used to propagate the electromagnetic (EM) energy through this turbulent flow, while meteorological parameters, such as temperature, humidity, and wind speed, are measured by co-located sensors. The phase noise self-cancellation and vibration isolation techniques are used to observe the scintillation down to millimeter length scales. The effect of temperature gradients and different mean wind speeds are shown to increase and shift the measured power spectrum of the radar signal within the inertial subrange and dissipation regions of turbulence. Results from this experimental setup are shown to be consistent and repeatable across multiple days. This setup can be used to: 1) investigate novel techniques for remote sensing of atmospheric turbulence; 2) develop statistical channel models for mmWave communication systems; and 3) expand on the existing scintillation theory.**

***Index Terms*—Atmospheric modeling, millimeter-wave (mmWave) propagation, scintillation, turbulence.**

I. Introduction

SCINTILLATION is defined as the random fluctuations of the amplitude and phase of an electromagnetic (EM) signal due to atmospheric turbulence. The shear forces in the atmosphere cause temperature and humidity gradients to undergo turbulent mixing, resulting in random fluctuations of the refractive index. Developing a better understanding and accurately modeling the effects of turbulence is essential for many applications. A powerful technique for remotely characterizing turbulence dynamics is by studying its effect on line-of-sight (LoS) EM signals. Statistical analyses of the scintillation reveal structural and dynamical information about turbulence in the propagation medium. Scintillation also has a significant impact on the accuracy and reliability of radar systems, aircraft safety, and satellite links. Furthermore, as telecommunications continue to advance toward higher frequencies to enable larger bandwidths and lower latency, atmospheric turbulence will play an increasingly critical role in the performance of these communication systems (see Fig. 1).

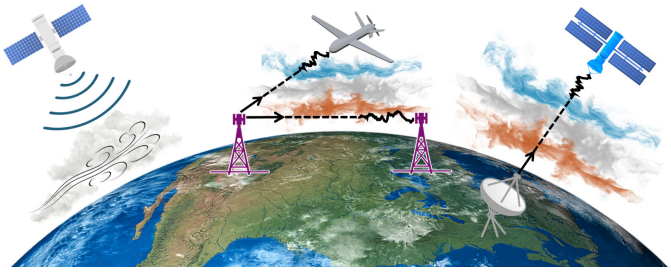

Fig. 1. Atmospheric turbulence impacts many applications.

Previous microwave scintillation experiments using terrestrial and satellite-to-ground links have been summarized in [1]. These measurement approaches showcase the logistical challenges of experimentally studying scintillation effects over long distances in the atmosphere, especially at millimeter wavelengths. In addition to the significant cost and capital required to establish these LoS propagation links, there is imperfect a priori knowledge of naturally generated turbulence, resulting in inconsistent and uncontrollable conditions. Furthermore, it is difficult to characterize meteorological parameters, as multiple concurrently operating in situ sensors need to be placed along the entire propagation path.

This article introduces a novel experimental setup for studying and characterizing atmospheric turbulence effects on the millimeter-wave (mmWave) propagation by using a versatile fan array wind tunnel (FAWT), located at the Center for Autonomous Systems and Technologies (CAST) at California Institute of Technology (Caltech). Each fan unit is individually programmable, allowing for a consistent and controlled

Received 8 September 2025; revised 20 February 2026; accepted 30 March 2026. Date of publication 20 April 2026; date of current version 9 July 2026. This work was supported in part by the Jet Propulsion Laboratory (JPL), Caltech, through National Aeronautics and Space Administration (NASA), under Contract 80NM0018D0004; and in part by the Caltech-JPL President's and Director's Research and Development Fund with support by RTX Corporation. *(Corresponding author: Shawn Sheng.)*

Shawn Sheng and Azita Emami are with the Department of Electrical Engineering, California Institute of Technology, Pasadena, CA 91125 USA (e-mail: ssheng@caltech.edu; azita@caltech.edu).

Omkar Pradhan, Simone Tanelli, and Ken Cooper are with the Jet Propulsion Laboratory, California Institute of Technology, Pasadena, CA 91125 USA (e-mail: omkar.pradhan@jpl.nasa.gov; simone.tanelli@jpl.nasa.gov; ken.b.cooper@jpl.nasa.gov).

Roni Goldshmid was with the Graduate Aerospace Laboratories, California Institute of Technology, Pasadena, CA 91125 USA. She is now with the Department of Aerospace Engineering, San Diego State University, San Diego, CA 92182 USA (e-mail: rgoldshmid@sdsu.edu).

Digital Object Identifier 10.1109/TAP.2026.3683991

0018-926X © 2026 IEEE. All rights reserved, including rights for text and data mining, and training of artificial intelligence and similar technologies. Personal use is permitted, but republication/redistribution requires IEEE permission.
See https://www.ieee.org/publications/rights/index.html for more information.

Authorized licensed use limited to: CALIFORNIA INSTITUTE OF TECHNOLOGY. Downloaded on September 21,2026 at 20:26:33 UTC from IEEE Xplore. Restrictions apply.

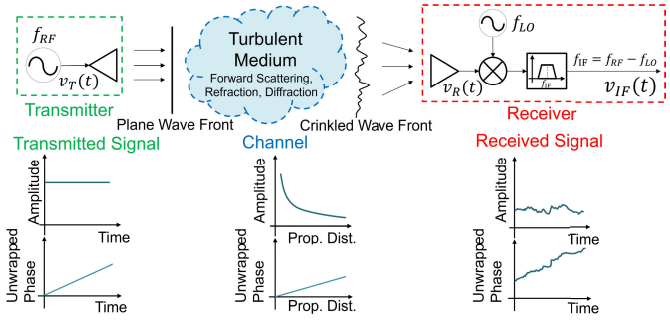

Fig. 2. Effect of turbulence on amplitude and phase of EM wave propagation in a typical heterodyne transceiver.

environment for repeatable experiments. The small-scale setup makes it more convenient for controlling and measuring meteorological parameters, such as temperature and wind speed to mimic different atmospheric conditions. Additions to this setup include a W-band (95.4 GHz) Doppler radar for radio frequency (RF) measurements, heavy-duty heaters for generating a large temperature gradient, as well as an infrared (IR) camera, hygrometers, and anemometers for meteorological measurements. The following sections of this article discuss: 1) the theory behind characterizing scintillations using meteorological parameters; 2) an overview of the experimental setup and measurement methodology; and 3) measurement results showing the influence of temperature gradients and wind speeds on the power spectrum of an RF signal.

II. Theoretical Analysis

Turbulence-induced scintillations in a propagating EM wave can be modeled as random amplitude and phase fluctuations (see Fig. 2). In this section, the received signal model and associated power spectral density (PSD) are introduced. The PSD is the main measured quantity used for statistical characterization of the signal, containing the combined effects of turbulence-induced scintillations and system noise. Analytical expressions relating meteorological and turbulent dynamics to measured amplitude and phase scintillations are outlined.

A. LoS Propagation Model for RF Scintillation

An EM signal in an LoS propagation link at the intermediate frequency (IF) output of a typical heterodyne receiver can be expressed as follows:

$$v_{IF}(t) = Ae^{\chi(t)}e^{j(2\pi f_{IF}t+\varphi(t)+\phi(t))} \tag{1}$$

where t is the time, A is the amplitude of the signal without scintillation, f_{IF} is the IF frequency, $\chi(t)$ and $\varphi(t)$ are the turbulence-induced log-amplitude and phase scintillations, respectively, and $\phi(t)$ is the system phase noise. In this experiment, the impact of $\chi(t)$ and $\varphi(t)$ on the received signal is observed and characterized. The primary frequencies of interest are close-in frequencies, which are predominantly affected by colored $(1/f)$ noise; therefore, white noise is neglected. In addition, the system amplitude noise is assumed to be minimal and is considered negligible.

B. Spectrum of Received Signal

In the lower troposphere, the weak scattering is assumed, which implies that $\langle\chi^2\rangle << 1$ and $\langle\varphi^2\rangle << 1$ [1]. The first-order Taylor expansion can thus be applied so that

$$v_{IF}(t) \approx A(1+\chi(t))e^{j2\pi f_{IF}t}(1+j\varphi(t))(1+j\phi(t)). \tag{2}$$

By calculating the autocorrelation function and applying the Wiener–Khinchin theorem, the PSD of the received IF signal is (see the Appendix)

$$\begin{aligned} S_{IF}(f) = A^2\big[&\big(\delta(f-f_{IF}) + S_\chi(f-f_{IF}) \\ &+ S_\varphi(f-f_{IF}) + S_\phi(f-f_{IF}) \\ &+ S_\phi(f-f_{IF}) * \big(S_\chi(f-f_{IF}) + S_\varphi(f-f_{IF})\big)\big]. \end{aligned} \tag{3}$$

The resulting PSD of the received signal is the sum of individual PSDs of the carrier, $\chi(t)$, $\varphi(t)$, and $\phi(t)$, as well as a convolution term. This convolution is typically orders of magnitude smaller than the previous terms and is assumed to be effectively negligible. In order to independently observe and characterize the effects of scintillation, its intensity must dominate over the system phase noise.

C. Spectrum of Turbulence-Induced Scintillation

For homogeneous and isotropic media in the lower troposphere, the PSDs for log-amplitude and phase scintillations (χ and φ, respectively), are given by [2], [3]

$$S_\chi(f) = 8\pi^2 Rk^2 \int_{2\pi f/v}^{\infty} \frac{d\kappa\kappa\Phi_n(\kappa)F_\chi(\kappa)}{\left(\kappa^2v^2-(2\pi f)^2\right)^{\frac{1}{2}}} \tag{4}$$

$$S_\varphi(f) = 8\pi^2 Rk^2 \int_{2\pi f/v}^{\infty} \frac{d\kappa\kappa\Phi_n(\kappa)}{\left(\kappa^2v^2-(2\pi f)^2\right)^{\frac{1}{2}}} \tag{5}$$

where $k = 2\pi f_{RF}/c$ is the wavenumber of propagation, f_{RF} is the RF carrier frequency, c is the speed of light in a vacuum, v is the mean wind speed, and f is frequency offset from the carrier. The function $F_\chi(\kappa)$ is the amplitude-variance spectral weighting function, and for plane waves is

$$F_\chi(\kappa) = \frac{1}{2}\left(1 - \frac{\sin\left(R\kappa^2/k\right)}{R\kappa^2/k}\right). \tag{6}$$

$\Phi_n(\kappa)$ is the refractive index wavenumber spectrum of irregularities and is defined as the Fourier transform of the spatial autocorrelation function of refractive index fluctuations

$$\Phi_n(\kappa) = \frac{0.033C_n^2}{(\kappa+\kappa_0)^{11/3}}\mathcal{F}(\kappa\eta) \tag{7}$$

where κ is the wavenumber, $\kappa_0 = 2\pi/L_0$ is the outer scale wavenumber of turbulence, L_0 is the outer scale length of turbulence, $\mathcal{F}(\kappa\eta)$ is the dissipation function, and η is the Kolmogorov microscale.

The term C_n^2 is the refractive index structure constant and quantifies the overall intensity of refractive index fluctuations. For homogeneous and isotropic media, the value of C_n^2 is the proportionality constant for the refractive index structure function in the inertial subrange

$$\left\langle\left[\delta n(r,t) - \delta n(r+\rho,t)\right]^2\right\rangle = C_n^2\rho^{\frac{2}{3}} \tag{8}$$

Authorized licensed use limited to: CALIFORNIA INSTITUTE OF TECHNOLOGY. Downloaded on September 21,2026 at 20:26:33 UTC from IEEE Xplore. Restrictions apply.

where δn is fluctuations of the refractive index n, r is the position in space, and ρ is the separation distance. In atmospheric settings, large propagation distances result in far stronger scintillation than is possible in the small-scale setup proposed here. Therefore, in order to observe the effect of scintillations in this laboratory setting, stronger refractive index fluctuations are needed. The values of C_n^2 in this particular setup are 10^4 times higher than those in natural conditions.

The observing system described in this work is fixed in space, while turbulent eddies are assumed to mainly translate orthogonal to the LoS between transmitter and receiver. Taylor's frozen flow hypothesis is applied here, which assumes that turbulent eddies are frozen as they move across the LoS propagation path. This allows for relating the space-wavenumber domain statistics (8) to time–frequency-domain statistics [see (4) and (5)] through the mean wind speed

$$\left\langle \left[\delta n\left(r,t\right)-\delta n\left(r+\rho,t\right)\right]^2\right\rangle = \left\langle \left[\delta n\left(r,t\right)-\delta n\left(r,t+\tau\right)\right]^2\right\rangle \quad (9)$$

where $\rho = v\tau$ and τ is the delay time.

D. Refractive Index Structure Constant C_n^2 Model

The vertical gradient approach is used to model C_n^2 [4]. This approach applies to conservative passive additives in a turbulent flow, which means that the additive does not change when the volume of air is shifted in space and does not affect the turbulent dynamics of the flow itself. For a conservative passive additive, the structure constant can be expressed as follows:

$$C_n^2 = a^2 L_o^{\frac{4}{3}} \left(\frac{\partial n}{\partial z}\right)^2 \quad (10)$$

where $a^2 = 2.8$ is a constant and z is the altitude. For microwave frequencies less than 100 GHz, the refractive index is related to meteorological parameters, as derived in [5]

$$n = 1 + \frac{77.6\times 10^{-6}}{T}\left(P + 4810\frac{e}{T}\right) \quad (11)$$

where T is the absolute temperature, P is the barometric pressure, and e is the water vapor partial pressure. However, T and e are not conservative quantities, but the potential temperature, $\theta = T(1000/P)^{0.286}$, and the specific humidity, $q = 0.622e/(P - 0.378e)$, are conservative. Simplifying $q = 0.622e/P$, the refractive index gradient can be calculated as follows:

$$\frac{\partial n}{\partial z} = -77.6\times 10^{-6}\frac{P}{T}\frac{\partial \ln\theta}{\partial z}\left(1 + 15\,600\frac{q}{T}\left(1 - \frac{1}{2}\frac{\frac{\partial \ln q}{\partial z}}{\frac{\partial \ln\theta}{\partial z}}\right)\right). \quad (12)$$

In this particular scenario, P is constant due to the lack of significant elevation. Furthermore, the specific humidity gradient is assumed to be negligible as no moisture is added or subtracted from the flow. The refractive index gradient can then be expressed as follows:

$$\frac{\partial n}{\partial z} = -77.6\times 10^{-6}\frac{P}{T^2}\left(1 + 15\,600\frac{q}{T}\right)\frac{\partial T}{\partial z}. \quad (13)$$

Therefore, by measuring T, P, and q, as well as the temperature gradient, the refractive index gradient and C_n^2 can be calculated. In this experimental setup, the total gradient orthogonal to the LoS propagation path is used instead of just the vertical component, which is dominant in the atmosphere from which this model is derived.

E. Turbulence Scales and Dissipation Region

For experiments carried out in CAST, the operating regime of the turbulent flow extends outside of the inertial subrange, the region of turbulence where there is an energy cascade as eddies begin to break down into smaller and smaller sizes due to inertial forces. Thus, higher wavenumbers and correspondingly higher temporal frequencies in the dissipation region must be considered, which is where turbulent eddies become too small and begin to dissipate into heat due to viscous forces. The $-5/3$ Kolmogorov spectrum power law for velocity fluctuations in the inertial subrange corresponds to a $-8/3$ power law for the log-amplitude and phase scintillation spectrum. However, in the dissipation region, the drop-off is exponential as the turbulent eddies become too small and dissipate into heat due to viscous forces [6]. The model for the velocity energy spectrum function is

$$E\left(\kappa_v\right) = C\varepsilon^{2/3}\kappa_v^{-5/3} f_\eta\left(\kappa_v\eta\right) \quad (14)$$

where $C = 0.5$ is the 1-D proportionality constant, κ_v is the velocity wavenumber, and ε is the turbulent energy dissipation rate. η is calculated as follows:

$$\eta = \left(\frac{\nu^3}{\varepsilon}\right)^{1/4} \quad (15)$$

where ν is the kinematic viscosity of air, which is a known constant for a given temperature. The model for $f_\eta(\kappa_v\eta)$ is

$$f_\eta\left(\kappa_v\eta\right) = e^{-\beta\kappa_v\eta} \quad (16)$$

with a constant $\beta = 5.2$.

For refractive index, which is a passive scalar, the dissipation function follows a similar exponential delay function:

$$\mathcal{F}\left(\kappa\eta\right) = e^{-\alpha\kappa\eta}. \quad (17)$$

The Hill bump model from previous optical experiments for temperature fluctuations uses an empirical value for $\alpha = 1.1090$, along with a fourth-order polynomial function to describe the effects of both kinematic viscosity and molecular diffusion operating at different scales [1]. For experiments presented in this work, the value of α is also determined empirically to model the dissipation region of refractive index fluctuations.

Calculations based on these models motivated the design and implementation choices for generating steep temperature gradients such that the turbulent medium causes signal scintillations which dominate over system phase noise. Furthermore, measuring these meteorological parameters along the propagation path is simpler in this experimental setting, and these equations can be used to calculate the expected PSDs of scintillation to be compared with experimental results.

Authorized licensed use limited to: CALIFORNIA INSTITUTE OF TECHNOLOGY. Downloaded on September 21,2026 at 20:26:33 UTC from IEEE Xplore. Restrictions apply.

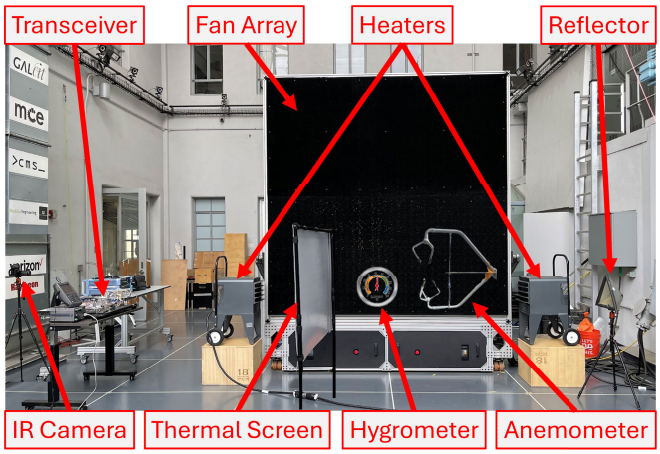

Fig. 3. Experimental setup in CAST showing: 1) fan array; 2) RF transceiver and reflector; 3) heaters for generating thermal gradients; and 4) meteorological sensors (for temperature, humidity, and wind speed measurements).

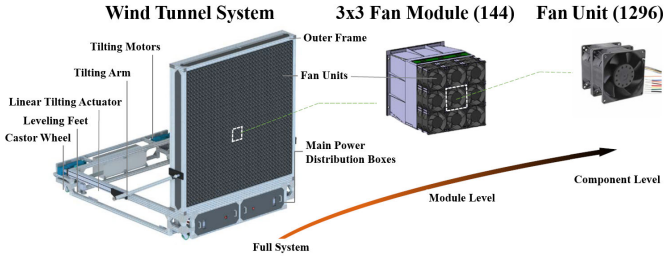

Fig. 4. CAST FAWT that is made up of 144 fan modules with each module consisting of a 3 × 3 array of individually programmable fans.

III. Experimental Overview

Scintillation experiments discussed in this work are conducted in Caltech's CAST facility (see Fig. 3) on a much smaller spatial scale than those reported previously [7], [8], [9]. This facility enables a simpler implementation of an otherwise logistically complex experimental effort. This experimental setup also facilitates finer control over turbulence generation, inclusion of high-resolution meteorological measurements, and experimental repeatability.

A. Fan Array Wind Tunnel

The CAST FAWT consists of an array of 36 × 36 individually programmable dual-fan units (see Fig. 4). Each unit consists of two counter-rotating fans that, along with a honeycomb mesh, create a swirl-free flow under uniform conditions. Each fan module can be programmed to generate spatiotemporally varying wind flows. The fan intensity is set by a corresponding duty cycle from 0% to 100%, with maximum wind speeds up to 15 m/s. Experiments presented here use a uniform flow at fan intensities up to 50% in 10% increments, corresponding to mean wind speeds of v =[2.1, 3.4, 5.0, 6.2, 7.3] m/s. Each fan unit is 80 × 80 mm, and the total array dimensions are 2.88 × 2.88 m. The overall facility is 15.2 × 9.1 × 12.2 m high.

B. mmWave Radar

To propagate mmWave EM energy through the flow generated by the FAWT, a W-band 95.4-GHz Doppler radar is employed, whose details are highlighted in [10]. The choice of this specific mmWave radar was mainly influenced by its ready availability at the Jet Propulsion Laboratory (JPL). The radar is not used for ranging, and is instead used as a single-tone continuous-wave (CW) transceiver, with specifications outlined in Table I. This transceiver consists of duplexing optics allowing use of a single-parabolic reflector for both transmit and receive. The far field for a reflector diameter of 15 cm and frequency of 95.4 GHz is >10 m, so the beam is highly collimated and assumed to be constant along the entire propagation path to simplify the analysis, and distance-dependent beam expansion is considered negligible. A trihedral reflector (Eravant SAJ-160-S1) is positioned approximately 5 m from the transceiver so that the propagation direction is orthogonal to the wind flow direction. This geometry may be considered a "folded" LoS propagation path. The transceiver system is placed on a vibration isolation platform (Newport VIP320X2430-00100) to minimize the effects of mechanical vibrations that contribute to system phase noise.

mmWave transceivers suffer from high-system phase noise. In this experiment, high close-in (near carrier) phase noise can drown out the turbulence-induced amplitude and phase scintillations (1)]. The transceiver system consists of a double heterodyning architecture (see Fig. 5) which mitigates this problem by: 1) taking advantage of strong self-cancellation of the 92.4- and 3.2-GHz local oscillator (LO) phase noise due to the short propagation path and co-located transmit–receive and 2) using an ultralow phase noise 200-MHz baseband (BB) source. The close-in phase noise self-cancellation can be better understood by noting that in a transceiver with common LO sources; the receiver phase noise is a time-shifted copy of the transmitter phase noise. The total receiver phase noise is

TABLE I
Specifications for the W-Band Transceiver Hardware

Parameter	Specification
Frequency	95.4GHz
Output Power	18dBm
Beam Diameter	15cm
Propagation Distance	10m

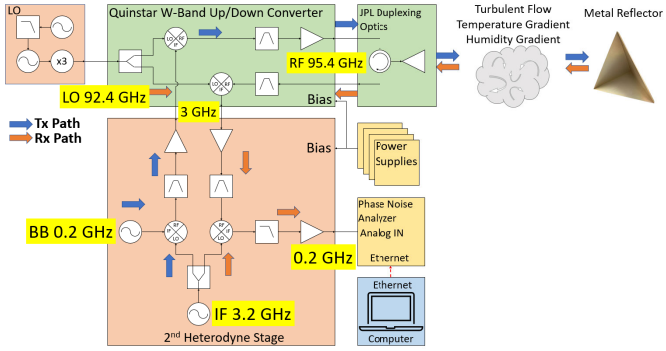

Fig. 5. Double heterodyne transceiver modulates the 92.4-GHz carrier with a 3.2-GHz IF signal, which in turn is modulated with a 0.2-GHz BB signal. The received signal is detected by a signal analyzer and used for PSD measurement.

Authorized licensed use limited to: CALIFORNIA INSTITUTE OF TECHNOLOGY. Downloaded on September 21,2026 at 20:26:33 UTC from IEEE Xplore. Restrictions apply.

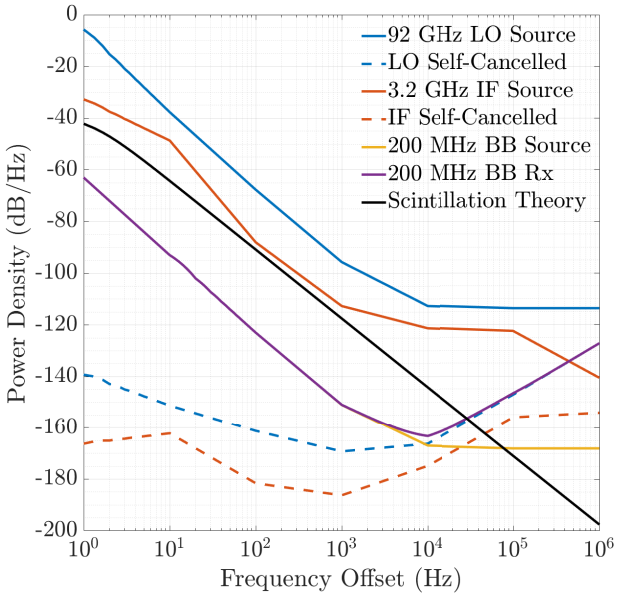

Fig. 6. Measured phase noise of carrier and modulating signals at transmitter and after self-cancellation in receiver in double heterodyne transceiver. Theoretical turbulence-induced scintillation for this setup is shown for comparison.

$$\begin{aligned}\phi(t) = {} & \phi_{LO}(t-\tau_R-\tau_2) - \phi_{LO}(t-\tau_2) \\ & + \phi_{IF}(t-\tau_1-\tau_R-\tau_2) - \phi_{IF}(t) \\ & + \phi_{BB}(t-\tau_1-\tau_R-\tau_2) \end{aligned} \tag{18}$$

where $\phi_{LO}(t)$, $\phi_{IF}(t)$, and $\phi_{BB}(t)$ are the phase noise of the W-band (92.4 GHz) LO source (Exodus Dynamics EDPLO-2000 with Eravant SFP-103KF-S2), IF (3.2 GHz) LO source (Valon 5009a), and BB (200 MHz) source (Wenzel 501-28309), respectively, τ_1 and τ_2 are propagation delays in the transmitter and receiver chains in the second heterodyne stage, respectively, and τ_R is the round trip propagation delay of the free-space folded LoS propagation link. Since the W band and IF heterodyne stages use common LO sources for transmit and receive, their phase noise is correlated, and thus self-canceled after the two down-conversions. The residual receiver system phase noise is thus dominated by the BB source at frequency offsets below 10^4 Hz, after which the LO self-canceled phase noise once again dominates at higher frequency offsets (see Fig. 6). By choosing an easily available ultralow phase noise BB source, the residual system phase noise can be kept below that of turbulence-induced amplitude and phase scintillations. It is important to note that the second heterodyne stage is necessary since the phase noise of a source that is hundreds of megahertz is significantly lower than the phase noise of sources in the gigahertz or mmWave range. This allows turbulence-induced scintillations to dominate at the receiver, resulting in better analysis and characterization.

C. Temperature

Heavy-duty utility heaters (King Electric PKB2015-3-P) are used to generate a large temperature gradient in the flow for observable scintillation. To measure the temperature, a plastic thermal screen is placed in front of the FAWT. The high emissivity of the plastic (0.84) allows it to closely mimic the temperature of the air, and an IR camera (FLIR T560) measures the resulting temperature profile of the flow. The limited resolution of the IR camera and the lagging thermal response of the plastic result in only snapshot temperature data being used, rather than video data to visualize the temperature in both temporal and spatial domains.

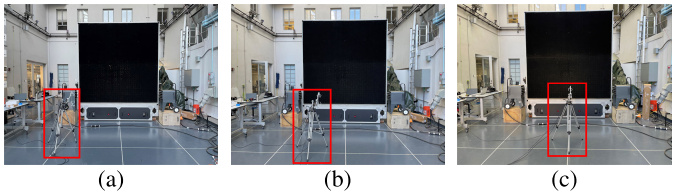

Fig. 7. Positioning of CTA with respect to the FAWT boundary, (a) at the edge, (b) 0.6 m from the edge, and (c) at the center.

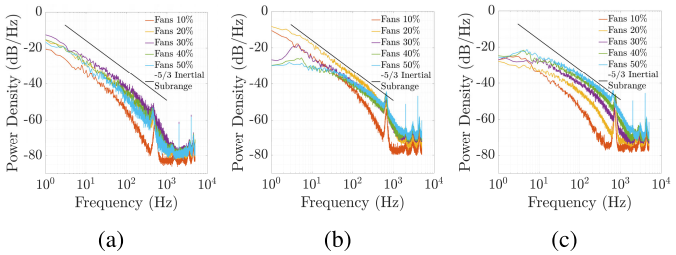

Fig. 8. PSD of wind speed fluctuations measured with CTA at (a) edge of FAWT, (b) 0.6 m from edge of FAWT, and (c) center of FAWT. Inertial subrange with −5/3 slope (black trace) is shown for comparison.

D. Wind Speed

Wind speed measurements are made using a sonic anemometer (Campbell Scientific CSAT3B) and a constant temperature anemometer (CTA) (Dantec Dynamics MiniCTA 54T42, with probe TSI 1201-20W). The sonic anemometer samples at 100Sa/s without the need for calibration, while the CTA samples at 10 kSa/s but require extensive calibration. The significant temperature fluctuations caused by the heaters make calibrating the CTA extremely challenging. By taking measurements with both anemometers in tandem, the values of the sonic anemometer are used as the ground truth for the CTA. A curve-fitting algorithm is applied to calculate the wind speed values of the CTA during postprocessing, eliminating the need for calibration [11], [12], [13].

IV. Measurement Results and Discussion

A. Wind Speed

The heaters have internal fans to blow the hot air, which are comparable in intensity to the FAWT at lower fan speeds. This creates variability in the turbulent dynamics of the flow along the propagation path of the beam, so the CTA is placed at multiple positions (see Fig. 7). At each position, for different fan speeds, 70-s sampling intervals are made, resulting in 700k samples per measurement. Following postprocessing of the data, the PSD of wind speed fluctuations is calculated using Taylor's frozen flow hypothesis (see Fig. 8). Spectral curve fitting is used to extract the local value of ε (14) at each position. A weighted average is then computed along the propagation path to obtain a representative ε. This averaged

Authorized licensed use limited to: CALIFORNIA INSTITUTE OF TECHNOLOGY. Downloaded on September 21,2026 at 20:26:33 UTC from IEEE Xplore. Restrictions apply.

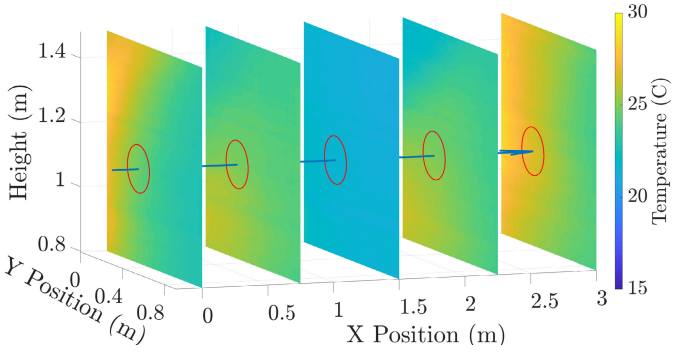

Fig. 9. Temperature profile of flow for fans at 20% duty cycle. The "X" position is with respect to the left edge of the FAWT shown in Fig. 7, and the "Y" position is downstream wind flow with respect to the face of the FAWT.

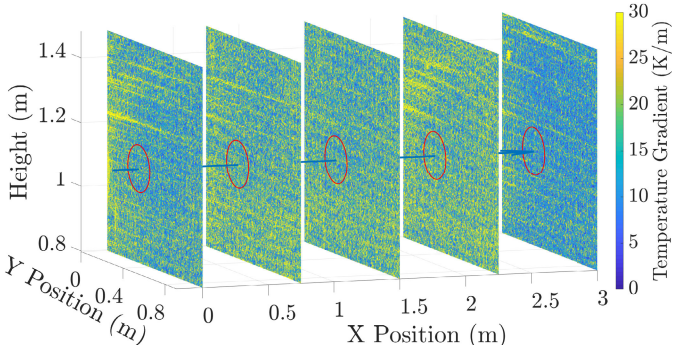

Fig. 10. Temperature gradient profile of flow for fans at 20% duty cycle. The "X" position is with respect to the left edge of the FAWT shown in Fig. 7, and the "Y" position is downstream wind flow with respect to the face of the FAWT. These profiles are used in the gradient model (13).

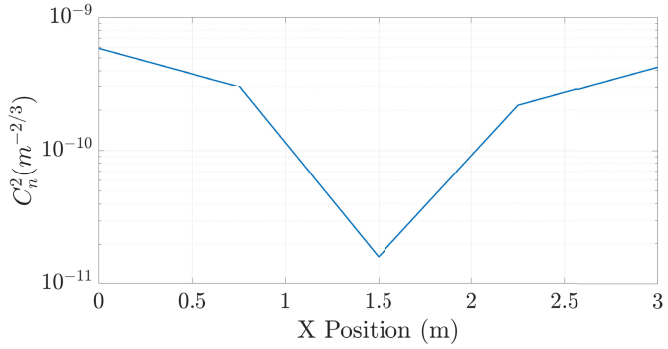

Fig. 11. Estimated C_n^2 at different positions in the flow using the gradient model (10). The "X" position is with respect to the left edge of the FAWT shown in Fig. 7.

value is used to calculate η (15), which is subsequently applied in the dissipation function of the scintillations PSDs (17). The low-Richardson number (<0.04) indicates that temperature behaves as a passive scalar and the flow is dominated by forced convection. Under these conditions, the ε values obtained from the CTA can be directly applied to the scintillation model.

B. Temperature

Snapshots of the temperature profile of the flow from the IR camera are taken at five positions for fan speeds from 0% to 50% in 10% increments. Sample measurements for

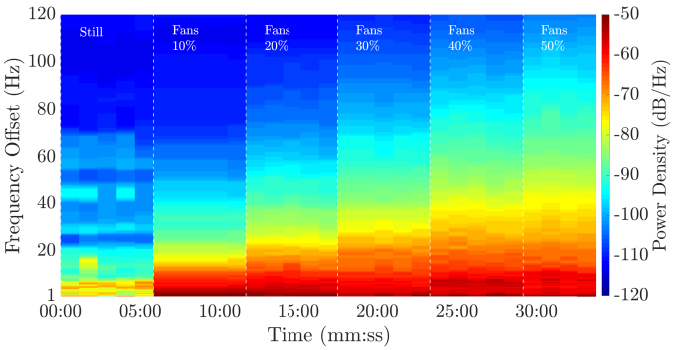

Fig. 12. Time series of measured PSD showing an increase in RF spectral energy at higher frequencies due to scintillations resulting from increasing fan speeds. The variance remains the same while the RF spectrum is spread over a wider range of frequencies due to smaller and faster moving eddies.

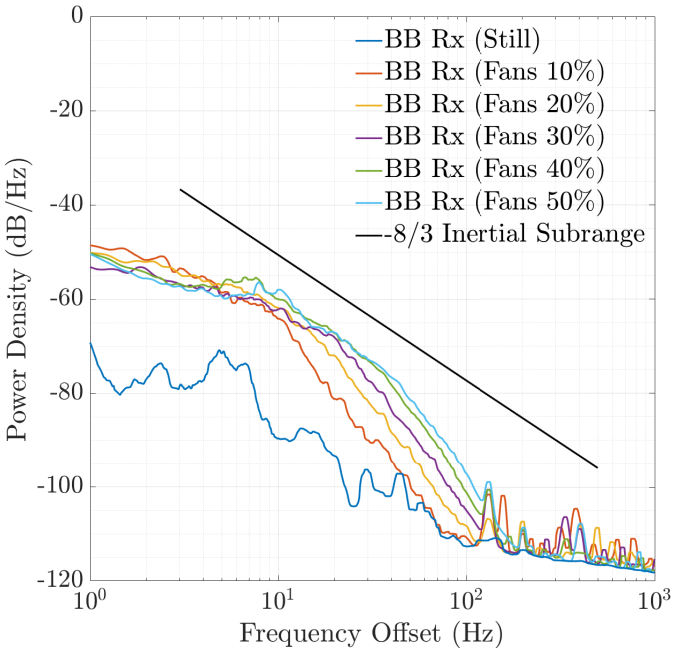

Fig. 13. PSD estimated from measurements averaged within each fan state shows the "rightward" shift of the spectrum due to increasing wind speeds. The mismatch of measured PSD with the typical −8/3 slope (black trace) of the inertial subrange indicates the breakdown of eddies in the dissipation region.

Fans 20% show a larger temperature increase at the edges of the FAWT closer to the heaters (see Fig. 9). The resulting temperature gradient is calculated at each pixel (see Fig. 10). The temperature gradient is averaged over the cross-sectional area of the collimated beam from the transceiver reflector to calculate the value of C_n^2 at each position (see Fig. 11). Since the magnitude of the temperature fluctuations is not constant across the entire propagation path, C_n^2 is integrated along the path and is assumed to be negligible for the area beyond the FAWT edges, since there is neither temperature gradient nor significant turbulent mixing.

C. Received Signal Power Spectrum

The PSD of the BB received signal is measured using a Rohde&Schwarz FSPN phase noise analyzer for different fan

Authorized licensed use limited to: CALIFORNIA INSTITUTE OF TECHNOLOGY. Downloaded on September 21,2026 at 20:26:33 UTC from IEEE Xplore. Restrictions apply.

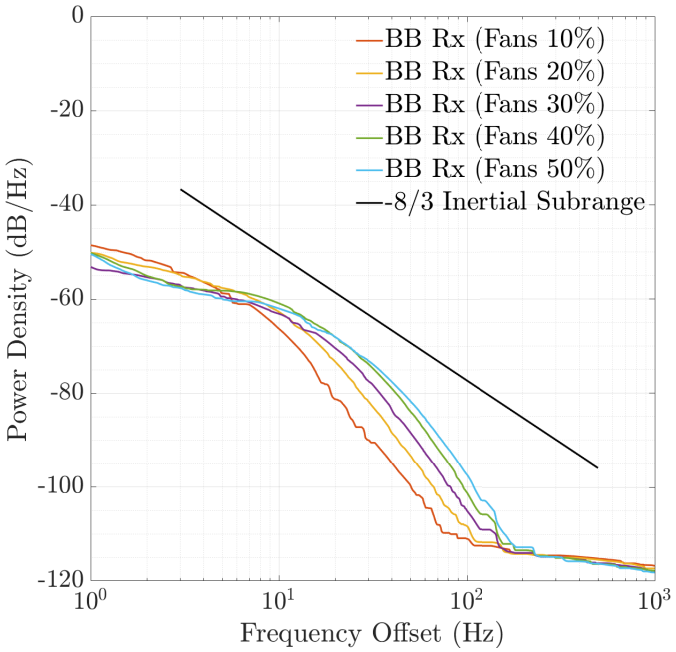

Fig. 14. Averaged PSD is smoothed with a "floor filter" to highlight the effect of increasing scintillations broadening the RF energy to higher frequencies.

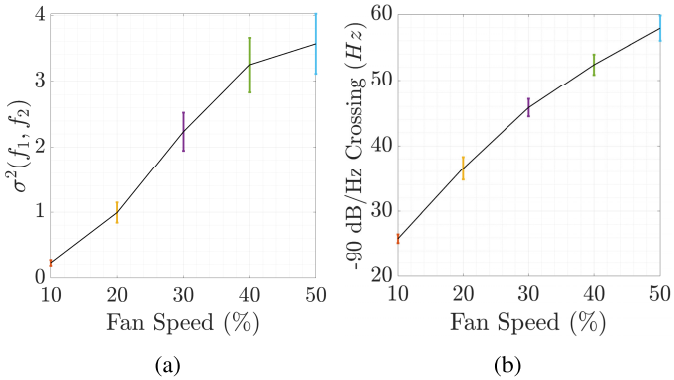

Fig. 15. Experimental repeatability is quantified with (a) bounded variance and (b) −90-dB/Hz PSD crossing point for each fan duty cycle, over 6 days. The error bars may be due to minor setup differences or changing background conditions such as ambient temperature, humidity, and wind.

speeds with heaters on the side. For each operating "state," five measurement samples are collected, each with a duration of 70 s (see Fig. 12). The five measurements of each state are averaged to give a representative PSD plot (see Fig. 13). The "still" state is when neither the heaters nor the FAWT are turned on and represents the residual oscillator phase noise at the receiver.

The introduction of a temperature gradient and turbulent mixing along the propagation path has a clear effect on the resulting PSD of the signal. The increase in spectral energy below 100 Hz can be attributed to the amplitude and phase fluctuations in the received signal caused by scintillation over and above those caused by system noise. Thus, these measurements showcase the sensitivity of the experimental setup to a turbulent propagation medium. Furthermore, increasing the fan intensity results in higher wind speeds that cause the spectrum to shift toward higher frequencies, which is supported by theory, as the faster mean wind speeds result in higher frequency turbulent eddies. These measurements also show different regions of turbulence. The turbulent eddies quickly enter the dissipation region, resulting in the steeper drop-off of the spectrum compared to the slope of −8/3 in the inertial subrange.

The slight increase of the PSD near 7 Hz for the higher FAWT speeds of 40%–50% are attributed to mechanical vibrations unfiltered by the vibration isolation platform, which has a 7-Hz resonant frequency. A custom floor filter, which keeps the minimum value of the PSD as the frequency is swept from low to high, is applied to the measured PSD to smooth out mechanical vibrations, as well as noise and other spurious signals. This takes advantage of the fact that scintillation effects are strictly decreasing with frequency, resulting in a better physical representation to isolate the effects of turbulence-induced scintillation (see Fig. 14).

D. Multiday Experiments

To verify the consistency and reliability of this laboratory setup, experiments are performed over 6 days while recreating an identical configuration on each day. Heaters are placed on the sides of the FAWT, and the transceiver is placed 1.7-m downstream. The measurement consistency is quantified using two metrics. The first is the integration of the received signal PSD across a truncated frequency range as a proxy for the variance. Integrating across all frequencies would theoretically produce the same value, since the variance for scintillation is independent of ν [2]. However, frequencies below 7 Hz do not provide a reliable measurement of the scintillation because of unfiltered mechanical vibrations at higher fan speeds. Therefore, an integration range between $f_1 = 20$ Hz and $f_2 = 100$ Hz relative to the carrier is chosen to isolate contributions from scintillation

$$\sigma^2(f_1, f_2) = \int_{f_1}^{f_2} PSD(f)\, df. \tag{19}$$

The statistics across multiple days show a clear increase with the fan speed [see Fig. 15(a)]. The standard deviation between experiments is attributed to day-to-day variations in the background environment and minor human error in resetting the experimental configuration. The larger deviation observed at fan speeds of 40%–50% is due to increased mechanical vibrations from the FAWT, which are not fully attenuated by the vibration isolation platform and therefore impact the sensitive integration calculation. The second metric is the frequency at which the PSD crosses −90 dB/Hz. For a fixed C_n^2, larger ν pushes the PSD toward higher frequencies. Thereofore, the −90 dB/Hz crossing point provides insight toward the overall mean wind speed of the flow [see Fig. 15(b)]. Both of these metrics demonstrate the consistency of this experimental setup across multiple days and can be used to develop a robust model to predict and provide insight toward the dynamics of the turbulent flow.

Authorized licensed use limited to: CALIFORNIA INSTITUTE OF TECHNOLOGY. Downloaded on September 21,2026 at 20:26:33 UTC from IEEE Xplore. Restrictions apply.

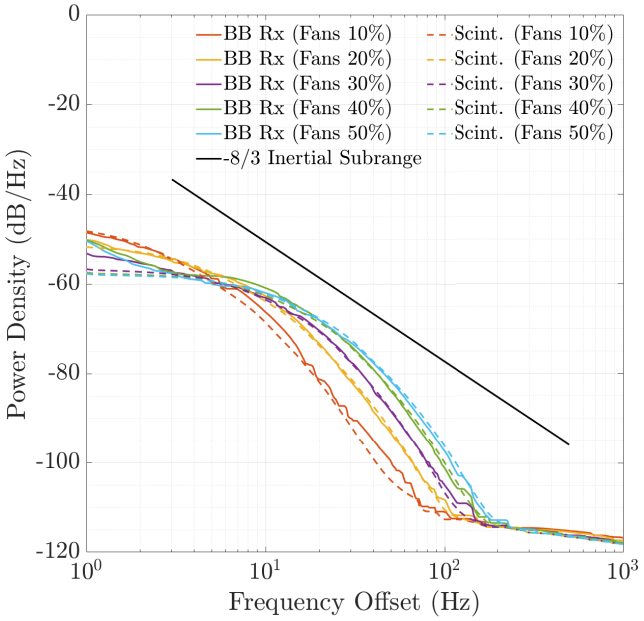

Fig. 16. Measured PSD (solid traces) versus scintillation theory (dashed traces), where the energy dissipation rate ε is estimated from CTA measurements in the presence of heaters (see Fig. 8). Inertial subrange with $-8/3$ slope is included for comparison.

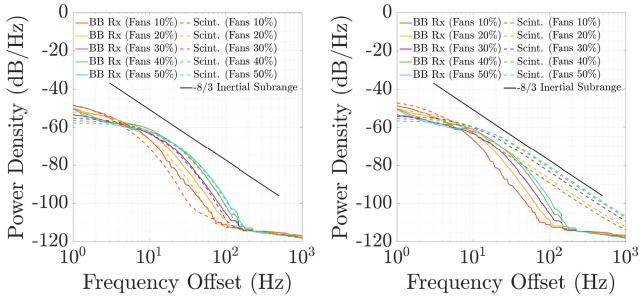

Fig. 17. Measured PSD (solid traces) versus scintillation theory (dashed traces), where (a) energy dissipation rate ε is estimated from CTA measurements in the absence of heaters and (b) model is calculated without the dissipation region using only the mean wind speed v. Inertial subrange with $-8/3$ slope is included for comparison.

E. Comparison With Theory

Using the measured values of C_n^2, v, and ε, theoretical PSDs of the log-amplitude and phase scintillations are numerically calculated [see (4) and (5)] and compared with the received signal measurements (see Fig. 16). An empirical value of $\alpha = 130$ provides a close fit between theory and measurement. Discrepancies at frequencies below 7 Hz are due to the unfiltered mechanical vibrations. Overall, the fit between theoretical PSDs and filtered measurements shows the accuracy of the model.

F. Influence of Heater Fans on Turbulence Spectrum

The scintillation effects due to temperature gradients and turbulent mixing with different wind speeds are clearly shown in the measurement results. Previous CTA measurements performed in the absence of the heaters result in lower values of ε at lower FAWT speeds. The influence of the fans within the heaters impacts the accuracy of the model [see Fig. 17(a)]. Furthermore, the measured PSD rapidly falls below the slope of $-8/3$ for scintillation in the inertial subrange [see Fig. 17(b)], showing that inclusion of the dissipation region is also necessary. These measurement results, along with the calculated scintillation theory, demonstrate the measurement detail required for the meteorological parameters to accurately model the received signal PSD.

G. Insights Into Turbulence From RF Measurements

The formation of a generalized model can be established as the overall shape of the scintillation curves is determined by C_n^2, L_o, v, and ε. Since C_n^2 and v can be measured more easily, the turbulence parameters L_o and ε can be extracted from the resulting received signal measurements. The regions where the PSD starts to fall off provide insight into the magnitude of ε. The modeling of the different turbulent regimes is also demonstrated and closely matches the measured plots. The characteristics of the measured spectrum enable remote sensing of the flow by revealing both the intensity of the scintillation and key structural and dynamical features of the turbulent medium. By developing an accurate scintillation model based on meteorological parameters, future measurements can be used to infer turbulence parameters, as the measured traces provide information about the underlying dynamics of the flow.

Additional experiments have been performed by placing the heaters in various positions relative to the FAWT, as well as moving the radar to different distances downstream. Similar measurement results have been achieved in multiple configurations depending on the wind speeds and overall temperature gradients. The configurability of this experimental setup demonstrates how robust it can be in collecting a wide array of data and studying various aspects of the flow.

V. Conclusion and Future Work

This article has introduced a novel approach for measuring and characterizing turbulence effects on mmWave propagation in a small-scale laboratory environment. Theoretical analysis is performed to support the design and implementation choices of the experiment. The use of the FAWT, along with several instruments for EM and meteorological measurements, allows experiments to be done in a consistent and controlled setting. Measurements are presented showing the effect of temperature gradients and wind speeds on the power spectrum of a 95.4-GHz signal that closely match theoretical scintillation models. The development of this experimental setup overcomes many of the challenges from previous studies that involved establishing an LoS propagation link over large distances, and directly links meteorological measurements with scintillation measurements to verify and augment existing theoretical models.

Future work can focus on enhancing the accuracy and sophistication of the measurement techniques. A natural extension of this work is to perform quantitative validation of the generalized model for remotely sensing turbulence

Authorized licensed use limited to: CALIFORNIA INSTITUTE OF TECHNOLOGY. Downloaded on September 21,2026 at 20:26:33 UTC from IEEE Xplore. Restrictions apply.

parameters L_o and ε from RF PSD measurements through direct comparison with ground truth CTA measurements. Developing an experimental configuration that ensures more uniform temperature gradients and turbulent dynamics along the entire propagation path will improve model reliability. Investigating the validity of Taylor's frozen flow hypothesis, as well as the assumptions of homogeneity and isotropy, will strengthen the foundational understanding of the flow. These aspects can be further evaluated to assess the feasibility of the proposed model under inhomogeneous conditions. In addition, the use of more sophisticated modulation schemes beyond a CW tone may enable expanded remote sensing capabilities in future work. Refining the quantitative analysis will allow for the development of a more precise and scalable application-specific model that can expand into real-world practices. Additional dynamics relating to scintillation can also be explored, such as the impact of fog and humidity gradients, different flow patterns (vortex shedding, shear flows, and turbulence at different scales) that better leverage the spatiotemporal programmability of the FAWT, and the impact of ambient conditions over diurnal shifts or seasonal changes. This experimental approach can extend to other applications to investigate different frequency bands and technologies such as multiple-input and multiple-output (MIMO) architectures.

Appendix
Derivation of IF Power Spectrum

The auto-correlation function of the received signal is

$$\begin{aligned} R_{IF}(\tau) &= \mathbb{E}\left[v_{IF}(t)\, v_{IF}^{*}(t-\tau)\right] \\ &= A^2 e^{j2\pi f_{IF}\tau}\mathbb{E}\big[(1+\chi(t))(1+\chi(t-\tau)) \\ &\quad \times (1+j\phi(t))(1-j\phi(t-\tau)) \\ &\quad \times (1+j\varphi(t))(1-j\varphi(t-\tau))\big]. \end{aligned} \tag{A.1}$$

Simplifications to $R_{IF}(\tau)$ can be made by first modeling $\chi(t), \phi(t), \varphi(t)$ as zero-mean random processes. Second, terms of the form $\mathbb{E}[\chi(\cdot)\phi(\cdot)]$ and $\mathbb{E}[\varphi(\cdot)\phi(\cdot)]$ are 0 because the processes related to scintillation are uncorrelated with the oscillator phase noise processes. Third, the log-amplitude and phase scintillation cross-terms cancel

$$\begin{aligned} \mathbb{E}\left[\chi(t)\varphi(t)\right] - \mathbb{E}\left[\chi(t-\tau)\varphi(t-\tau)\right] &= 0 \\ \mathbb{E}\left[\chi(t-\tau)\varphi(t)\right] - \mathbb{E}\left[\chi(t)\varphi(t-\tau)\right] &= 0. \end{aligned} \tag{A.2}$$

The scintillation processes are assumed to be stationary, and they are real processes; thus, their cross-correlation function is real and even about the origin. Finally, it is assumed that higher order moments of the form $\mathbb{E}[\chi(\cdot)\chi(\cdot)\varphi(\cdot)]$, $\mathbb{E}[\chi(\cdot)\varphi(\cdot)\varphi(\cdot)]$, and $\mathbb{E}[\chi(\cdot)\chi(\cdot)\varphi(\cdot)\varphi(\cdot)]$ are much smaller compared with the second-order moments and thus can be ignored. From the above assumptions, $R_{IF}(\tau)$ can be simplified and written in terms of the auto-correlation functions of each individual process

$$\begin{aligned} R_{IF}(\tau) = A^2 e^{j2\pi f_{IF}\tau}\big(1 &+ R_{\chi}(\tau) + R_{\varphi}(\tau) + R_{\phi}(\tau) \\ &+ R_{\phi}(\tau)\left(R_{\chi}(\tau) + R_{\varphi}(\tau)\right)\big). \end{aligned} \tag{A.3}$$

Using the Wiener–Khinchin theorem, the PSD is

$$\begin{aligned} S_{IF}(f) = A^2\big[&\big(\delta(f-f_{IF}) + S_{\chi}(f-f_{IF}) \\ &+ S_{\varphi}(f-f_{IF}) + S_{\phi}(f-f_{IF}) \\ &+ S_{\phi}(f-f_{IF}) * \left(S_{\chi}(f-f_{IF}) + S_{\varphi}(f-f_{IF})\right)\big]. \end{aligned} \tag{A.4}$$

Acknowledgment

The authors would like to thank Dave Sar and Dave Manzi of RTX for their inputs and expertise.

References

[1] A. D. Wheelon, "Waves in random media," in *Electromagnetic Scintillation*, vol. 1. Cambridge, U.K.: Cambridge Univ. Press, 2001.
[2] A. D. Wheelon, "The temporal variation of phase," in *Electromagnetic Scintillation*, vol. 1. Cambridge, U.K.: Cambridge Univ. Press, 2001.
[3] A. D. Wheelon, "The power spectrum and autocorrelation," in *Electromagnetic Scintillation*, vol. 2. Cambridge, U.K.: Cambridge Univ. Press, 2003.
[4] E. Martini, A. Freni, F. Cuccoli, and L. Facheris, "Derivation of clear-air turbulence parameters from high-resolution radiosonde data," *J. Atmos. Ocean. Technol.*, vol. 34, no. 2, pp. 277–293, 2016. [Online]. Available: https://journals.ametsoc.org/view/journals/atot/34/2/jtech-d-16-0046.1.xml
[5] E. Smith and S. Weintraub, "The constants in the equation for atmospheric refractive index at radio frequencies," *Proc. IRE*, vol. 41, no. 8, pp. 1035–1037, Aug. 1953.
[6] S. B. Pope, "The scales of turbulent motion," in *Turbulent Flows*. Cambridge, U.K.: Cambridge Univ. Press, 2000.
[7] R. W. McMillan, R. A. Bohlander, R. J. Hill, and S. F. Clifford, "The effects of turbulence in clear and turbid atmospheres on millimeter wave propagation," *Proc. SPIE*, vol. 1039, pp. 162–163, Nov. 1988, doi: 10.1117/12.978384.
[8] K. A. Norton et al., "An experimental study of phase variations in line-of-sight microwave transmissions," Nat. Inst. Standards Technol., Gaithersburg,MD, USA, Tech. Rep., 1961, doi: 10.6028/NBS.MONO.33.
[9] K. L. Ho, N. D. Mavrokoukoulakis, and R. S. Cole, "Propagation studies on a line-of-sight microwave link at 36 GHz and 110 GHz," *IEE J. Microw.*, vol. 3, no. 3, p. 93, 1979, doi: 10.1049/ij-moa.1979.0022.
[10] K. B. Cooper et al., "A compact, low power consumption, and highly sensitive 95 GHz Doppler radar," *IEEE Sensors J.*, vol. 20, no. 11, pp. 5865–5875, Jun. 2020.
[11] E. Kit and B. Grits, "In situ calibration of hot-film probes using a collocated sonic anemometer: Angular probability distribution properties," *J. Atmos. Ocean. Technol.*, vol. 28, no. 1, pp. 104–110, Jan. 2011. [Online]. Available: https://journals.ametsoc.org/view/journals/atot/28/1/2010jtecha1399_1.xml
[12] E. Kit, A. Cherkassky, T. Sant, and H. J. S. Fernando, "In situ calibration of hot-film probes using a collocated sonic anemometer: Implementation of a neural network," *J. Atmos. Ocean. Technol.*, vol. 27, no. 1, pp. 23–41, Jan. 2010. [Online]. Available: https://journals.ametsoc.org/view/journals/atot/27/1/2009jtecha1320_1.xml
[13] R. H. Goldshmid, E. Winiarska, and D. Liberzon, "Next generation combined sonic-hotfilm anemometer: Wind alignment and automated calibration procedure using deep learning," *Experim. Fluids*, vol. 63, no. 1, p. 30, Jan. 2022, doi: 10.1007/s00348-022-03381-1.

Shawn Sheng (Student Member, IEEE) received the B.A.Sc. degree in electrical engineering from the University of Waterloo, Waterloo, ON, Canada, in 2019, and the M.S. degree in electrical engineering from California Institute of Technology, Pasadena, CA, USA, in 2020, where he is currently pursuing the Ph.D. degree in electrical engineering.

Authorized licensed use limited to: CALIFORNIA INSTITUTE OF TECHNOLOGY. Downloaded on September 21,2026 at 20:26:33 UTC from IEEE Xplore. Restrictions apply.

Omkar Pradhan (Senior Member, IEEE) received the B.E. degree from the University of Mumbai, Mumbai, India, in 2009, and the M.S. and Ph.D. degrees in electrical engineering from the University of Colorado Boulder, Boulder, CO, USA, in 2013 and 2019, respectively.

He is currently an RF/MW Engineer at the Microwave Systems and Technology Group, NASA's Jet Propulsion Laboratory (JPL), Pasadena, CA, USA. His research interests include RF remote sensing instrument design for Earth and planetary sciences and atmospheric propagation measurements.

Roni Goldshmid received the B.S. degree from the University of California, Berkeley, Berkeley, CA, USA, in 2012, and the M.S. and Ph.D. degrees from Technion—Israel Institute of Technology, Haifa, Israel, in 2016 and 2020, respectively.

She is a former Caltech Presidential Post-Doctoral Fellow and a Rising Star at Stanford University, Stanford, CA, USA. She is currently an Assistant Professor at the Department of Aerospace Engineering, San Diego State University, San Diego, CA, USA. Her research focuses on fluid structure interactions, heat transfer, and flow control to address the complex challenges of aerial wildfire suppression. Her current interests include developing advanced experimental and theoretical models, creating predictive statistical tools for wind–fire–vegetation interactions, and designing data-driven optimization algorithms for aerial firefighting operations. By integrating fundamental scientific principles, advanced machine learning techniques, and cutting-edge aerodynamic systems, she aims to enhance the safety, efficiency, and effectiveness of aerial firefighting operations.

Dr. Goldshmid was a recipient of the Grinshpen Prize for Excellence in Environmental Engineering.

Simone Tanelli received the Ph.D. degree in remote sensing from the University of Florence, Florence, Italy, in 1999.

He was a Principal Scientist of the RainCube InVEST technology demonstration. He is currently an INCUS Project Scientist at JPL, Pasadena, CA, USA. He has more than 20 years of experience in research and development of atmospheric active and passive remote sensing measurement systems and methods.

Ken Cooper (Senior Member, IEEE) received the A.B. degree in physics from the Harvard College, Cambridge, MA, USA, in 1997, and the Ph.D. degree in physics from California Institute of Technology, Pasadena, CA, USA, in 2003.

He is currently an RF Microwave Engineer at the Submillimeter Wave Technology Group, Jet Propulsion Laboratory, California Institute of Technology, focusing on the development of ground, airborne, and space-based millimeter- and submillimeter-wave radar and heterodyne spectroscopy systems for Earth science, planetary science, and security.

Azita Emami (Senior Member, IEEE) received the B.S. degree from the Sharif University of Technology, Tehran, Iran, in 1996, and the M.S. and Ph.D. degrees in electrical engineering from Stanford University, Stanford, CA, USA, in 1999 and 2004, respectively.

From 2004 to 2006, she was with the IBM Thomas J. Watson Research Center, Yorktown Heights, NY, USA. She joined California Institute of Technology (Caltech), Pasadena, CA, USA, in 2007, where she is currently the Andrew and Peggy Cherng Professor of electrical engineering and medical engineering and the Director of the Center for Sensing to Intelligence. She was the Executive Officer (Head) of the Department of Electrical Engineering from 2017 to 2024. Her current research interests include integrated circuits and systems, integrated photonics, wearable and implantable devices for neural recording, neural stimulation, sensing, and drug delivery.

Dr. Emami was an IEEE Solid-State Circuits Society (SSCS) Distinguished Lecturer from 2017 to 2018. From 2016 to 2021, she was an Associate Editor of IEEE JOURNAL OF SOLID-STATE CIRCUITS (JSSC).

Authorized licensed use limited to: CALIFORNIA INSTITUTE OF TECHNOLOGY. Downloaded on September 21,2026 at 20:26:33 UTC from IEEE Xplore. Restrictions apply.